HiSST: 3rd International Conference on
High-Speed Vehicle Science & Technology
14–19 April 2024, Busan, Korea

Heat Flux Augmentation Caused by Surface Imperfections in Turbulent Boundary Layers

William Ivison[1], Chris J. Hambidge[1], Matthew McGilvray[1], Alan Flinton[2], Jim Merrifield[2], Johan Steelant[3]

Abstract

Aerodynamic heating of hypersonic vehicles is one of the key challenges needed to be overcome in the pursuit of hypersonic ascent, re-entry, or sustained flight. Small, unavoidable imperfections are always present on the surface of aircraft in the form of steps, gaps, and protuberances. These can lead to high levels of localised heat flux augmentation, up to many times the undisturbed level. Flat plate experiments have been carried out in the Oxford High Density Tunnel with the aim of characterising the heating effects caused by small scale protuberances and steps in turbulent boundary layers. The current work presents experimental heat flux augmentation data, an assessment of existing heat flux correlations, and introduces new engineering level correlations to describe heat flux augmentation for a range of surface geometries.

Keywords: *heat flux, hypersonic, correlation, step, protuberance*

Nomenclature

Latin

B – IR camera calibration constant [K]
BF – Bump Factor (= HFA)
C – Transmissivity conversion constant [-]
c_p – Constant pressure heat capacity [J kg^{-1} K^{-1}]
F – IR camera calibration constant [-]
G – IR camera calibration constant [counts]
H – Height (of step or cavity) [m]
HDT – High Density Tunnel
HFA – Heat Flux Augmentation [-]
L – Length (of cavity) [m]
M – Mach number [-]
p – Pressure [Pa]
Pr – Prandtl number [-]
R – IR camera calibration constant [counts]
Re – Reynolds number [-]
S – Cavity shape factor [-]
St – Stanton number [-]
T – Temperature [K]
u – Velocity [m s^{-1}]
U – IR signal [counts]
X – Correlation axis [-]
Y – Correlation axis [-]

Greek

δ – Boundary layer thickness [m]
ϵ – Emissivity [-]
γ – Ratio of specific heat capacities [-]
λ – Wavelength [m]
ρ – Density [kg m^{-3}]
τ – Transmissivity [-]
θ – Momentum thickness [m]

Subscripts

0 – Stagnation condition
amb – Ambient
atm – Atmospheric
cal – IR calibration
D – Detector (of IR camera)
obj – Object of interest
rec – Recovery
$shot$ – During a tunnel shot
w – Condition at the wall

[1] *Oxford Thermofluids Institute, University of Oxford, OX2 0ES. Corresponding author email address: william.ivison@eng.ox.ac.uk*
[2] *Fluid Gravity Engineering Ltd., Emsworth, PO10 7DX*
[3] *ESA-ESTEC, Keperlaan 1, 2200 AZ Noordwijk, Netherlands*

Copyright © 2024 by the author(s)

1. Introduction

There is a need for engineering tools capable of simplifying the complex interactions between different components and quickly assessing the performance of vehicle designs to allow for quick changes between design iterations [1, 2, 3]. These tools aim to provide surface quality and interface tolerances to avoid unwanted onset of transition or the creation of hot spots and overheats. In the past this was assessed manually at some critical points [4]. However, recent developments have been aimed towards automatic assessment over the complete external surface using empirical correlations, such as transition onset or local overheats. This helps to define needed tolerances for machine drawings or to indicate whenever a reusable vehicle requires a refurbishment of its external surface before a reflight [5, 6, 7].

Several studies have been carried out in recent years which have shown strong correlations between levels of heat flux augmentation, the physical scale of surface defects, transition onset, and local flow properties. Studies by Everhart [8, 9] have characterised the expected heating rates on cavities initially at flow conditions experienced by the Shuttle TPS and also later with boundary layer edge conditions applicable to hypersonic cruise. Similar work by Hollis [10] has characterised the heat flux augmentation caused by cavities on the heatshield of the Orion capsule. Estruch [11] produced correlations describing heat flux in the vicinity of angled protuberances at hypersonic cruise conditions. All of these studies have produced easily useable correlations from high quality experimental data. However, while being valuable tools, the use of this type of empirical correlation is restricted to the geometries and flow conditions with which they were generated. Therefore, an extension to the library of high quality experimental heat flux augmentation data using conditions suited to hypersonic cruise trajectories, and realistic geometries, is an asset for vehicle design.

This paper follows on from initial experiments presented in Ivison et al. [12], focusing in particular on heat flux augmentation in the vicinity of surface geometries. Additionally, numerical work has been carried out to better understand the flow fields around these geometries [13].

2. Experimental Setup

2.1. Experimental Model

The experimental model used was a sharp flat plate, 575 mm in length and 300 mm in width. The model allowed a wide range of 2-dimensional surface geometries to be reproduced with high precision. The upper surface of the model was made up of two independently actuated blocks: an upstream ”fence” block located at an axial position of 150 mm and 5 mm in running length and 140 mm in width; and a downstream ”step” plate which was located at an axial position of 155 mm, 390 mm in running length and 110 mm in width. The key benefit of using two blocks in this configuration was that it allowed different combinations of steps, gaps, and protuberances to be tested with ease.

In order to obtain data for a large range of different geometries, the model incorporated two remotely operated Thorlabs PIA25 piezoelectric actuators to move the blocks creating the surface geometries. The actuators were fixed in a horizontal orientation to the rear plate and moved the front block vertically relative to the rear plate via an arrangement of linear slides. Figure 1 shows layout and overall construction of this mechanism. The inclusion of remotely operated actuators avoided the need for manual access to the model which would require repressurisation of the facility, allowing efficient turn-around between tests.

Tested geometries were categorised by the relative heights of each actuated block. Possible permutations are displayed in Table 1, showing a description, code, and schematic of the model. The codes correspond to the height difference moving between each part of the model and subscripts signify the height relative to the fixed upstream portion of the plate. For example: UF represents an upwards change followed by no change (flat) - a forward-facing step; and DU$_-$ represents a downward change followed by an upward change lower than the fixed plate - a backward-facing step with an intermediate gap. For each of the listed geometry types, multiple sizes were tested, with geometries of most interest receiving the most tests.

Copyright © 2024 by the author(s)

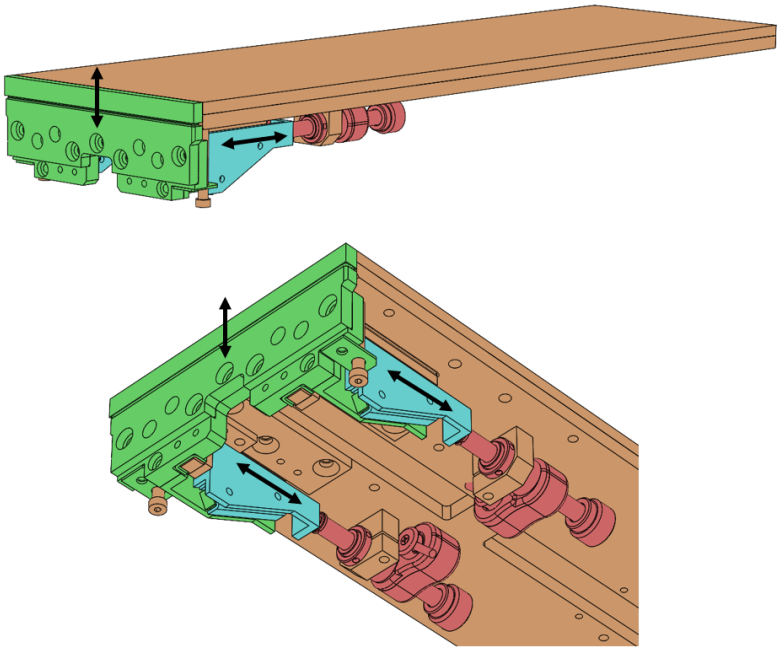

Fig 1. Two CAD views of the model mechanism, showing how the motion of the actuators (red) is transmitted to the front block (green).

2.2. Instrumentation

A variety of instrumentation was implemented into the model design to measure: surface heat flux in the vicinity of the test geometry; an assessment of the boundary layer state; freestream properties; and the height of each block making up the test geometry. A picture of the model with instrumentation indicated is given in Figure 2.

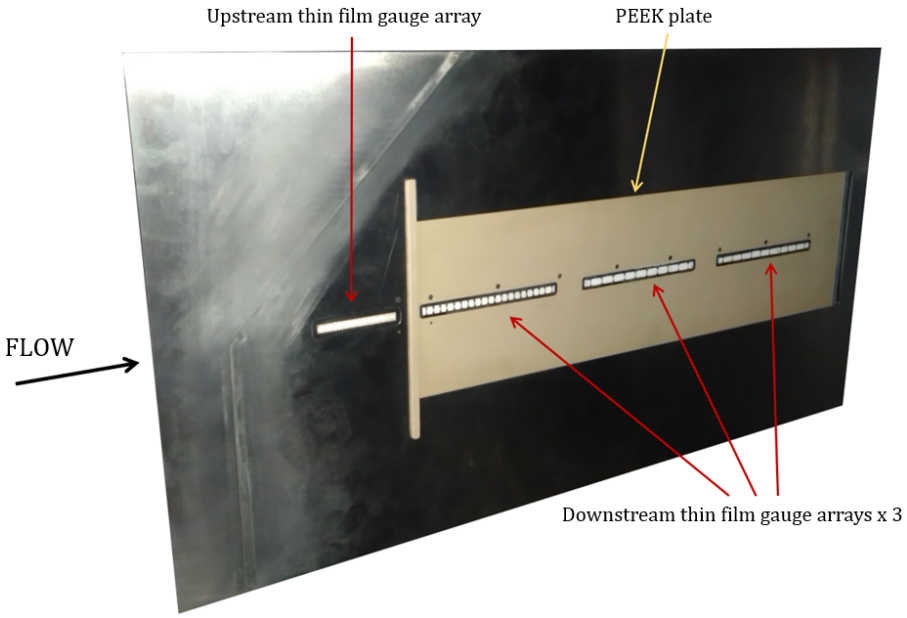

Fig 2. The experimental model with instrumentation indicated.

Copyright © 2024 by the author(s)

Table 1. Categorisation of different geometries

Description	Code	Diagram
Flat plate	FF	
Fence	UD_F	
Forward-facing step	UF	
Forward-facing step	FU	
Backward-facing step	DF	
Backward-facing step	FD	
Double step forward	UU	
Double step backward	DD	
Fence-step forward	UD_+	
Fence-step backward	UD_-	
Step-gap forward	DU_+	
Step-gap backward	DU_-	
Gap/cavity	DU_F	

2.2.1. IR Thermography

IR thermography was the primary measurement used for this work, providing a high spatial resolution for heat flux measurements. A Telops M3k FastCam was used to view MWIR in the range 1.5 - 5.2 µm. Both the actuated blocks which made up the test geometry were manufactured from PEEK, which has an emissivity of 0.93. The camera recorded a windowed frame of 320 x 128 pixels at 4000 frames per second with an integration time of 90 µm. The camera was positioned outside the test section and viewed the model through a 5 mm thick sapphire window with an anti-reflective coating. A 50 mm lens was used to view the vicinity of the fence/step location and produced images with a pixel size of ~0.4 mm. The camera was oriented so that the incident angle was less than 50° – this is the approximate limit at which the emissivity of an insulator can be assumed to be constant [14].

Fundamental Concepts

The total amount of electromagnetic radiation emitted from a black body is described by Planck's Law, the wavelength form of which is shown in Equation 1:

$$I_s(\lambda) = \frac{2\pi hc^2}{\lambda^5} \cdot \frac{1}{\exp\left(\frac{hc}{\lambda k_B T}\right) - 1} \tag{1}$$

Where I_s is the emitted intensity of radiation per unit wavelength, h is the Planck constant, c is the speed of light in a vacuum, and k_B is the Boltzmann constant. The sensors which make up the focal plane array (FPA) of an IR camera directly measure incident radiation. This means that the measured camera signal, U, can be described by an equation of the same form as Planck's Law:

Copyright © 2024 by the author(s)

$$U = \frac{R}{e^{B/T} - F} \tag{2}$$

Where the constants $R, B,$ and F are all a function of the optical system. In reality, the radiation measured by the camera is made up of contributions from other sources in addition to the object of interest. The two main additional components come from radiation reflected from the object being measured and radiation being emitted from objects in the optical path - primarily from the atmosphere and any windows being used. Emissivity and transmissivity terms can also be included to account for the fact that the object being measured is not a black body and that the optical path does not transmit all emitted radiation. A more complete equation describing the IR setup is given by Astarita [15], shown in Equation 3:

$$U_D = \epsilon_{obj}\tau_{atm}\frac{R}{e^{B/T_{obj}} - F} + (1-\epsilon_{obj})\tau_{atm}\frac{R}{e^{B/T_{reflect}} - F} + (1-\tau_{atm})\frac{R}{e^{B/T_{atm}} - F} \tag{3}$$

The terms on the right-hand side of Equation 3 describe, in order: the emitted radiation from the object of interest; the radiation from the environment which is reflected from the object of interest; and the emitted radiation from the atmosphere. The temperatures with subscripts $reflect$ and atm refer to the temperature reflected from the object of interest and the temperature of the atmosphere, respectively. During calibrations and shots, these temperatures are both the ambient temperature of the system and remain constant. This reduces the last two of the three terms in Equation 3 to constants which can replaced by a single constant, G, as proposed by Zaccara et al. [16].

IR Calibration Procedure

To calibrate the IR system, a CI Systems SR-33N-7A extended area blackbody calibrator was placed in the test section in place of the experimental model. The calibrator consists of a flat surface of size 178 x 178 mm which can be set to specified temperatures. The emissivity is given as 0.98, the spatial uniformity is given as 0.01 K, and the temperature accuracy is given as 0.05 K. During calibration, the blackbody was set to a number of temperatures spanning the range of surface temperatures expected during model testing. Images were recorded at each temperature set-point, giving data points for camera measurement, U, as a function of observed temperature for the particular optical system. The calibration equation is given in Equation 4.

$$U_{D,cal} = \frac{R}{e^{B/T_{cal}} - F} + G_{cal} \tag{4}$$

This is analogous to Equation 3 with the last two terms being absorbed into the constant G. The constants $R, B, F,$ and G are determined by fitting Equation 4 to the U and T_{cal} data on a pixel-by-pixel basis. The Levenberg-Marquardt least squares fitting method is used.

If an in-situ calibration is carried out (where all properties of the optical system are kept constant between the calibration and the test), the emissivity and transmissivities of the optical system can be ignored. For this work, a so-called semi in-situ calibration was performed [17]. This involves a calibration using the majority of the optical setup as is used in the shot but with a change in total transmissivity of the system. The total transmissivity changes due to the fact that the calibration is carried out in ambient air, whereas shots use nitrogen as the test gas. Atmospheric air contains significant quantities of CO_2 and water vapour which absorb heavily in MWIR. The total radiated intensity is also affected by the material being observed: materials with higher emissivities emit more IR radiation for a given temperature. These factors all have an influence on the measured counts from the camera. Equation 5 describes the measured IR signal during a shot:

$$U_{D,shot} = \frac{CR}{e^{B/T_{shot}} - F} + G_{shot} \tag{5}$$

Copyright © 2024 by the author(s)

Where C is a constant which converts between calibration and shot optical systems, defined by Equation 6.

$$C = \frac{\epsilon_{shot}\tau_{shot}}{\epsilon_{cal}\tau_{cal}} \tag{6}$$

The difference in transmissivity between calibrations and shots is entirely caused by the difference in test section gas composition. This reduces the ratio τ_{shot}/τ_{cal} to a value of 0.9764. Transmissivity data for atmospheric air and nitrogen was generated using the online tool, SPECTRA [18], created by Mikhailenko et al. [19]. Values of emissivity are 0.98 and 0.93 for the calibrator and PEEK model surface, respectively. The resulting value of C is 0.9266.

The constant G_{shot} in Equation 5 is different to G_{cal} in Equation 4 due to the differences in optical setup and ambient temperature. In order to assess the magnitude of G_{shot}, two assumptions are made: the value of G_{shot} remains constant for the duration of the shot; and the pre-shot surface temperature of the model is the same as the measured ambient temperature. G_{shot} can then be defined by Equation 7:

$$G_{shot} = U_{D,pre-shot} - \frac{CR}{e^{B/T_{amb}} - F} \tag{7}$$

Applying this to Equation 5 and rearranging for object temperature results in Equation 8, which provides a relationship between the measured camera signal and the temperature of the object of interest during a shot.

$$T_{obj} = \frac{B}{\ln\left(\frac{CR}{U_{D,shot} - U_{D,pre-shot} + \frac{CR}{e^{B/T_{amb}} - F}} + F\right)} \tag{8}$$

2.2.2. Thin Film Gauges

In addition IR thermography, thin film heat transfer gauges were used to measure heat flux. These were mounted in arrays on the centreline of the model and, in this work, were primarily used to confirm that the boundary layer was turbulent upstream of the test geometry. The gauges consisted of thin layers of platinum painted onto a Macor substrate with gold strips providing an electrical connection to cabling. The gauges operate as RTDs and were pre-calibrated to allow for conversion between the measured gauge resistance and the gauge temperature.

2.2.3. Heat Flux Calculation

Heat flux is calculated using temperature data from IR thermography and thin film gauges. The change in temperature with time is converted to surface heat flux using a 1D semi-infinite heat transfer assumption and an impulse response method developed by Oldfield [20].

2.2.4. Geometry Height Measurement

The height of the manually adjusted rear plate was measured using an RS PRO digital dial indicator at multiple locations around the perimeter of the plate during height adjustments. The gauge had an accuracy of ±5 µm. The height of the remotely actuated front block was measured using two Alps Alpine RDC1014A09 linear potentiometers: one measuring the height next to a single actuator. The response of the potentiometers were pre-calibrated using the dial indicator.

2.2.5. Freestream Characterisation

The stagnation pressure was measured using a Kulite XCQ-080-70BARA pressure sensor, with a measurement uncertainty of 0.5 % of the full scale output of 70 bar. A pitot probe was mounted on the underside of the model and consisted of a Kulite XCQ-093-100A sensor, also with a measurement uncertainty of 0.5 % of its full scale output of 100 psi (∼700 kPa). Kulites were amplified using Fylde FE-H379-TA transducer amplifiers which applied a low pass filter with a cutoff frequency of 30 kHz to the signals.

Copyright © 2024 by the author(s)

Total temperature measurements were carried out using an aspirated thermocouple, mounted alongside the pitot probe. The aspirated thermocouple consists of a thermocouple suspended across a hollow cylinder and uses approximations of a cylinder in cross-flow to calculate the total temperature of the freestream.

The model was aligned with the flow using a model alignment probe, also mounted on the underside of the model, beneath the leading edge. The probe consists of a small blunted cone with four Kulite XCEL-152-25A sensors positioned at cardinal points. By comparing opposite pressure measurements, the alignment of the model can be assessed.

2.3. The Oxford High Density Tunnel

Shown in Figure 3, the HDT consists of a 152.4 mm diameter x 17.4 m long, electrically heated barrel capped, on the downstream end, by a pneumatically operated fast-acting plug valve. A contoured nozzle sits downstream of the plug valve via an intermediate plenum. Nozzles exist for Mach numbers of 4, 5, 6, and 7 which can be interchanged as necessary. All nozzles have a 0.351 m exit diameter and exit into a free jet test section which leads to a dump tank of volume 28 m^3. HDT typically operates as a Ludwieg tunnel, where the barrel is pressurised and heated to the required amount before venting through the nozzle. This produces periods of steady flow of between 30 and 50 ms depending on the condition. In addition to standard Ludwieg mode operation, a piston stroke can be incorporated into the firing sequence to further heat the test gas [21], and the dynamics of the plug valve can be tuned to extend test times [22]. For further details on the construction and operation of HDT, see McGilvray [23] & Wylie [24]. For data presented in this work, the Mach 6 nozzle and Ludwieg mode operation were used.

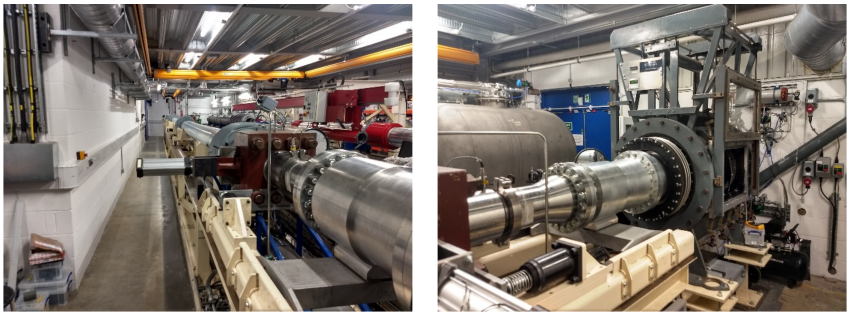

Fig 3. The Oxford High Density Tunnel (HDT).

2.4. Test conditions

Conditions were chosen which created a turbulent incoming boundary layer on the fence geometry at a running length of 150 mm. Table 2 shows details of the conditions used. Conditions B and C transitioned naturally at distances of around 100 and 80 mm, respectively. For Condition A, a boundary layer trip was used, consisting of a 1 mm diameter wire being affixed to the plate at a distance of 40 mm, causing the boundary layer to transition at around 80 mm. Turbulent boundary layer heights were estimated using a virtual origin at the transition location.

Table 2. A summary of the test conditions used.

Condition	M	p_0 [bar]	T_0 [K]	Re_{unit} [10^6/m]	δ_{fence}, mm	# of tests
A	6.14	18.1	435	16.4	2.71	10
B	6.13	27.1	433	24.8	2.03	41
C	6.17	37.6	436	33.5	2.34	10

Copyright © 2024 by the author(s)

3. Results

3.1. Heat flux augmentation

Results are presented as a non-dimensionalised heat flux augmentation (HFA) to observe changes in behaviour when compared with undisturbed smooth wall heating. This is defined as:

$$HFA = \frac{\mathrm{St}}{\mathrm{St}_{flat}} \cdot \left(\frac{\mathrm{Re}_{unit\ flat}}{\mathrm{Re}_{unit}} \right)^{1/5} \tag{9}$$

Where St is the Stanton number, defined as:

$$\mathrm{St} = \frac{q}{\rho_e u_e c_p (T_{rec} - T_w)} \tag{10}$$

Where T_{rec} is the recovery temperature, defined as:

$$T_{rec} = T_e (1 + \sqrt{\mathrm{Pr}_e} (\frac{\gamma - 1}{2}) M_e^2) \tag{11}$$

Freestream conditions between nominally identical shots vary by < 1%. To account for this small variation, the heat flux ratio is multiplied by the ratio of Re_{unit} between the two shots, raised to the power $1/5$. This exponent comes from Eckert's turbulent heat flux correlation [25].

When moving the fence and step into a flat plate configuration, a small vertical offset between the different sections of the plate often occured. This was always measured to be < 20 µm (less than 1% of the boundary layer thickness), so any downstream effects were determined to be negligible. However, small hot and cold spots were present in the heat flux profiles - up to an 8% deviation from the correct level. As these were to be used for normalisation, any deviations from the true flat plate heat flux would produce non-physical artefacts in the resulting heat flux augmentations. Eckert's heat flux correlation was used, instead of the IR data, as the flat plate Stanton number. Figure 4 shows IR data compared with the correlation.

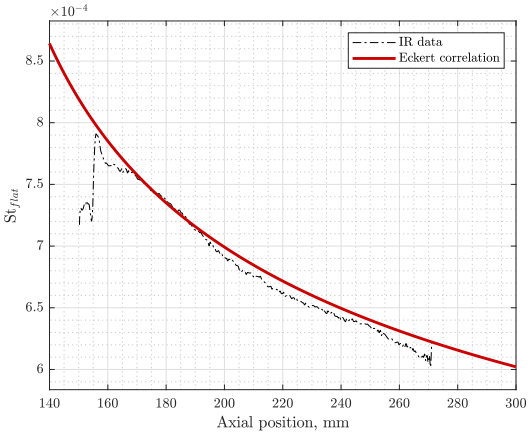

Fig 4. Flat plate IR data for Condition B.

3.2. Heat Flux Profiles for Basic Geometries

In each of the plots in this section, the heat flux augmentation profile is plotted against axial position as a distance from the model leading edge. For each profile, a schematic diagram of the geometry is given, along with the heights of the fence and step components relative to the upstream plate listed in the legend. Geometries are also shown in which a change in behaviour was observed when testing different geometry scales.

Copyright © 2024 by the author(s)

3.2.1. Forward-Facing Steps

Experimental heat flux augmentation data for a forward-facing step (FU) is shown in Figure 5a. At location of the step, $x = 155$ mm, there is a peak in heat flux, which decreases rapidly at first and steadily relaxes to the flat plate level. Upstream of the step, a separation bubble creates an increased plateau in heat flux at an intermediate level between the baseline and the peak, which then increases again up to the peak. This plateau begins at around $x = 140$ mm after rising over the preceding ~10 mm. The rise is visible in thin film gauge data (crosses) but the plateau is located between the thin film gauges and IR data. The location of the end of the plateau is captured in the IR data at around $x = 152$ mm, where the heat flux begins to rise to its peak.

3.2.2. Backward-Facing Steps

Experimental heat flux augmentation data for a backward-facing step (DF) is shown in Figure 5b. A separation directly behind the step causes a sudden drop in heat flux. The shape of the heat flux as it recovers back to a steady level is dependent on the ratio of the step height to the boundary layer thickness. Typically, larger steps cause an overshoot in heat flux at the reattachment location. In this dataset, step heights were large enough to produce only a small overshoot. Due to a thinner boundary layer following reattachment, the downstream heat flux is greater than the flat plate level.

3.2.3. Fences (2-Dimensional Protuberances)

A 2-dimensional protuberance (protuberances can also be defined with a 3rd width dimension), or fence, (UD_F) can be thought of as a forward-facing step followed by a backward-facing step. The same features as each isolated step are present in the heat flux profile, with similar dependencies on step height. The heat flux peaks on the leading edge of the fence, decreases towards the trailing edge, and drops due to a separation in the wake of the fence. Similarly to backward-facing steps, the reattachment causes an overshoot if the fence is high enough compared to the boundary layer. Figure 5c shows the heat flux on two fence geometries of different heights: 0.2 mm and 2.0 mm. Compared to the larger fence, the smaller fence has a lower peak heat flux, a smaller decrease in heat flux in the separated region and doesn't overshoot the flat plate level at reattachment. The larger fence also causes a decrease in the recovered level following the reattachment overshoot. The 2.00 mm fence in Figure 5c displays a large overshoot whereas the backward-facing step of the same size in Figure 5b shows no overshoot. This suggests a dependency on the flow upstream of a backward-facing step when looking at flow reattachment.

3.2.4. Cavities

As with fences, cavities (DU_F) can be viewed as a backward-facing step followed by a forward-facing step. Cavities in this work are all categorised as open cavities - with L/H < 10 [26]. The flow over open cavities separates but does not fully establish again on the floor before it reaches the downstream corner. This leads to the heat flux profile shown in Figure 5d. The cavity floor experiences a drop in heat flux, caused by a separation, which increases along the length of the cavity to the peak augmentation level on the upper edge of the downstream face. The heat flux downstream of the cavity relaxes to a level close to the flat plate baseline.

3.3. Heat Flux Profiles for Combined Geometries

In addition to the four simple geometries above, a number of combined cases were tested.

3.3.1. Double Forward-Facing Steps

Steps with smaller intermediate steps will be referred to as double steps. The heat flux profiles for forward-facing double steps (UU geometries) compared with that of a single step of the same total height are shown in Figure 6a. The inclusion of an intermediate step creates an additional hot spot. It can be seen that the relative heights of each step are important: the smaller intermediate step of 0.46 mm increases the peak HFA value (now at $x = 155$ mm rather than $x = 150$ mm) compared to the larger intermediate step of 1.00 mm in which the second peak is lower than the first. In all three cases, the initial peak is approximately the same height, indicating that the heat flux on double steps primarily affects downstream heat loads. The heat flux upstream of double steps was not measured in this work, so any differences in upstream separation cannot be speculated. Note that the small bump in the blue profile at $x = 155$ mm is due to the interface between the two adjustable blocks.

Copyright © 2024 by the author(s)

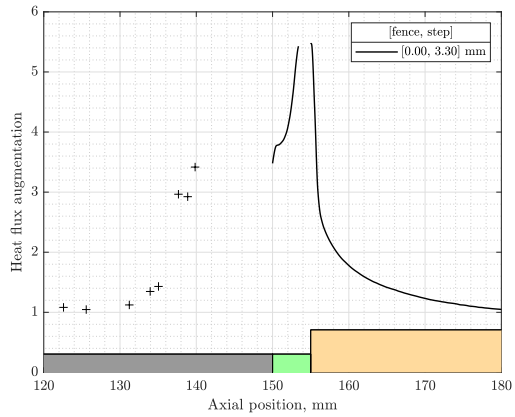

(a) Forward-facing steps.

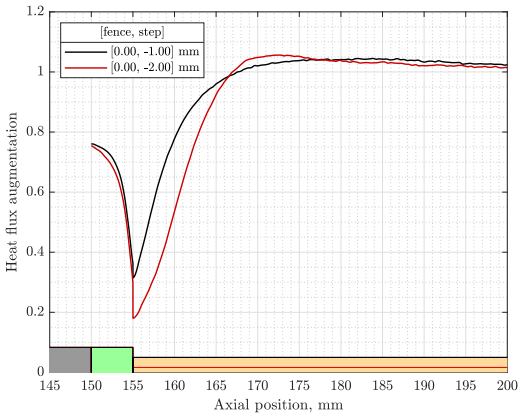

(b) Backward-facing steps.

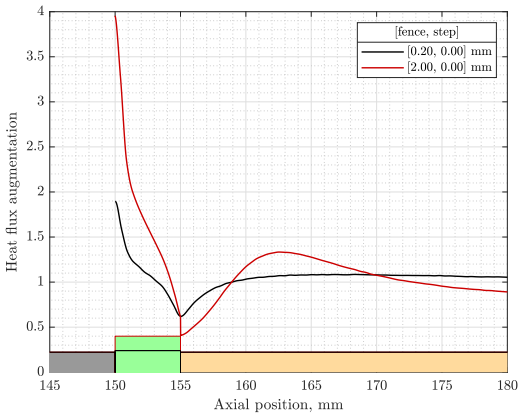

(c) Fences.

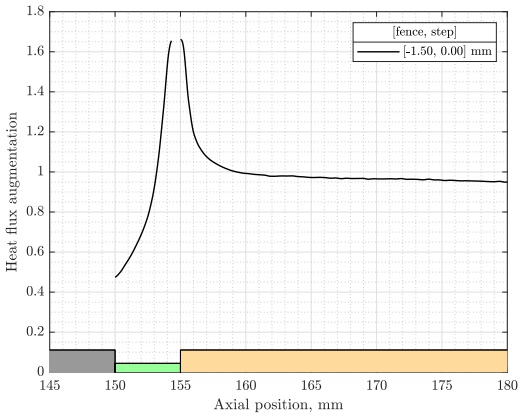

(d) Cavities.

Fig 5. Heat flux augmentation for basic geometries at tunnel Condition B.

3.3.2. Double Backward-Facing Steps

Heat flux profiles for a backward-facing step compared with two heights of double backward-facing step are presented in Figure 6b. Compared to the single step (in blue), intermediate steps appear to extend the overall separation length. At both step locations ($x = 150$ and $x = 155$ mm) a larger change in height creates a more pronounced separation and a lower minimum heat flux. The most downstream of these steps, at $x = 155$ mm, has a larger impact on the overall heat load experienced by the model.

3.3.3. Steps with Intermediate Fences

Figure 6c shows three fences with differing rear drop heights. The flow field over all three of the geometries is similar until $x = 155$ mm, causing the heat flux profile across the top of the fences ($x = 150$ - 155 mm) to be identical in each case. The heat flux in the downstream separation is directly affected by the drop height, with the larger downward steps causing larger separations, greater reattachment heating, and lower minimum heat flux in the internal corner of the rear step.

In contrast, Figure 6d shows heat flux profiles for two different fence heights and one flat fence (FD geometry), all with a $\sim$1 mm drop at $x = 155$ mm. In this case, the flow fields are substantially different to each other further upstream compared to the fences shown in Figure 6c. Even with similar sized downward steps, the overall heat flux profiles are completely different. Larger initial steps cause a higher level of heat flux in the entire vicinity of the fence: the blue 2.50 mm height line is consistently

Copyright © 2024 by the author(s)

higher than the red 1.00 mm line until about $x = 170$ mm. However, the location of the reattachment overshoot, and therefore the size of the separation, appears to be the same for each step. In contrast to the fences, the rear-facing step (in black) has a completely different profile, not overshooting at reattachment and settling at a higher heat flux further downstream.

3.3.4. Forward-Facing Steps with Upstream Gap

The effect of including a recess upstream of a forward-facing step (DU_+ geometries) is examined in Figure 6e. Any size of upstream cavity appears to cause a separation over the cavity, which reduces the local heat flux, including that on the peak of the step at $x = 155$ mm. Above a cavity depth of 0.5 mm, there is no additional reduction of heat flux caused by further increasing the depth. Additionally, the downstream effect of these cavities is negligible, with almost identical heat flux profiles immediately downstream of the step. This result may be useful in vehicle design, where the addition of a small cavity upstream of a step could be used to reduce the integrated heat flux in an area without impacting the downstream flow.

3.3.5. Backward-Facing Steps with Downstream Gap

Intermediate cavities were also tested on backward-facing steps (DU_- geometries). Figure 6f shows two backward facing step-gaps compared to a single step, all with an overall step height of -1 mm. Similarly to the forward step-gaps shown in Figure 6e, the inclusion of an intermediate cavity reduces the heat flux in the cavity itself. Small hot spots occur on the downstream lip of the cavity at $x = 155$ mm, but not to a level of heat flux higher than the single step. Further downstream, the heat flux profiles recover to the same level within around 15 mm. Once again, this may be a useful result from the perspective of vehicle design.

3.4. Correlation Development

Various quantities of interest can be extracted from data presented in the above figures, for example: peak heating on the corner of a forward facing step or minimum heating in the separation after a backward facing step. The magnitudes of these quantities are determined by local flow properties, geometry scale, and the type of geometry. As such, correlations can be developed to describe the relationships between relevant quantities.

The correlation formulated by Everhart [9] to describe various heating quantities in 3-dimensional cavities is shown in Equation 12. Variables X and Y are defined using flow and geometric quantities and are then fitted to a straight line.

$$X = \ln\left[M_e^{\sigma} Re_{\theta}^{\tau} \left(\frac{L}{\delta}\right)\right] \tag{12a}$$

$$Y = \ln\left[\left(\frac{H}{\delta}\right)^{\alpha} \left(1 + \frac{L}{H}\right)^{\beta} BF\right] \tag{12b}$$

$$Y = a + bX \tag{12c}$$

Where, L is the length of the cavity, H is the height of the cavity, and BF is the "bump factor" - analogous to HFA. Re_{θ} is the Reynolds number based on the local momentum thickness. The value of momentum thickness used to calculate this is approximated as $\theta = 0.097\delta$ [27]. The constants α, β, σ, τ, a, and b are calculated by fitting the function to experimental data. Fitted constants for the average bump factor on the floor of open cavities are listed in Table 3.

Table 3. Constants for average open cavity floor bump factor, taken from Everhart [9].

α	β	σ	τ	a	b
3.70	2.70	0.00	0.10	-2.3741	2.6034

Applying this correlation to the current dataset indicates that this method is not applicable to combined stepped cavity geometries. Figure 7a shows average HFA for cavity-type geometries plotted according

Copyright © 2024 by the author(s)

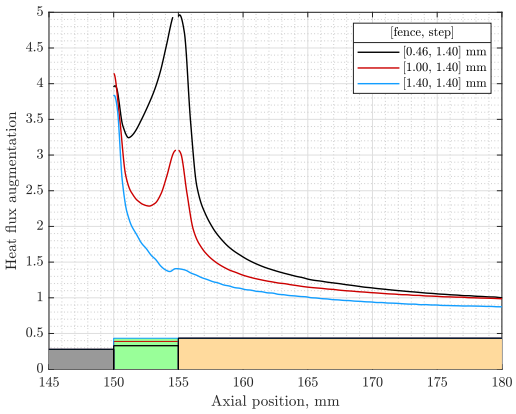

(a) Double forward-facing steps compared with a single forward-facing step.

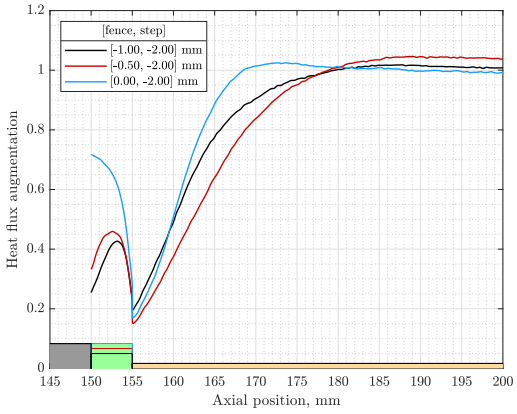

(b) Double backward-facing steps compared with a single backward-facing step.

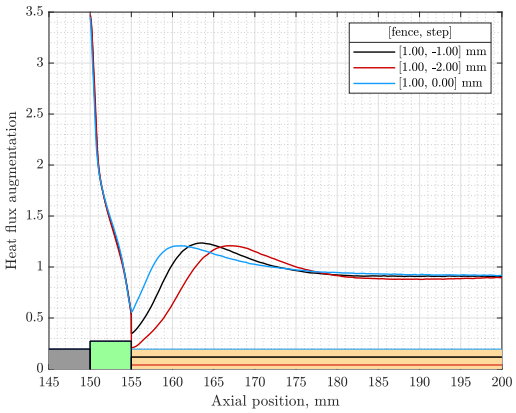

(c) 1 mm height fences with different rear plate heights.

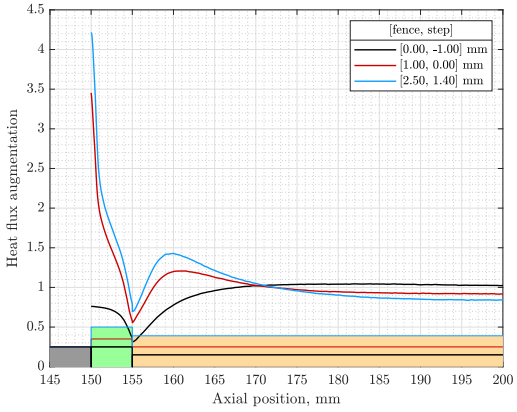

(d) 1 mm drop heights following different upstream fence heights.

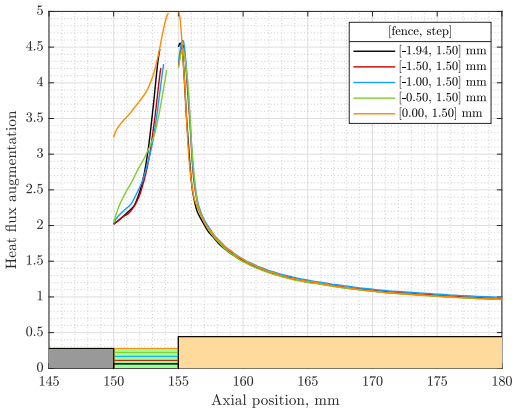

(e) Forward-facing steps with upstream cavities of different depths.

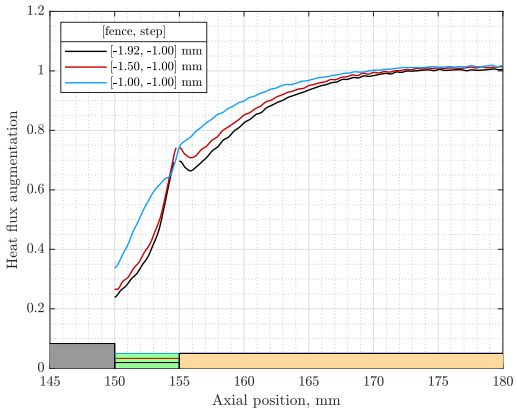

(f) Backward-facing steps with downstream cavities of different depths.

Fig 6. Heat flux augmentation for combined geometries at tunnel Condition B.

Copyright © 2024 by the author(s)

to Equation 12. Geometries included in this figure are (referring to Table 1): DU_F, DU_+, and DU_-. Data points are coloured according to the height of the rear plate, H_2 (see Figure 8). Medium-blue points, corresponding to plate heights of 0 mm (DU_F), can be compared with Everhart's dataset. These points generally lie the closest to the central line, indicating that the correlation is applicable to 2-dimensional cavities as well as 3-dimensional cavities. However, geometries with different rear plate heights deviate significantly and do not appear to follow a trend.

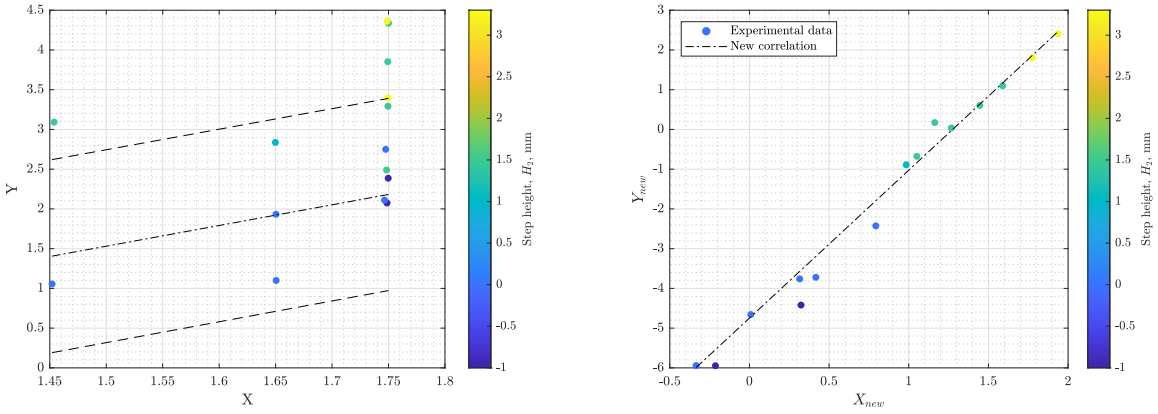

(a) Equation 12 using constants in Table 3.

(b) Equation 13 using constants in Table 4.

Fig 7. Data applied to correlations for average cavity floor heating.

The current dataset tested flow conditions at a single Mach number (M = 6) and geometries of a single length (L = 5 mm), resulting in a small range in X. The variety of geometry types and scales tested (and therefore range of HFA) leads to larger range in Y. To make this correlation scheme more applicable to combined geometries, various modifications were made to Equation 12 to account for the different entrance and exit heights of geometry configurations. The modified correlation scheme is shown in Equation 13.

$$X_{new} = \ln\left[M_e^{\sigma} Re_{\theta}^{\tau}\left(\frac{|\Delta H|}{\delta}\right)\right] \tag{13a}$$

$$Y_{new} = \ln\left[\left(\frac{|\Delta H|}{\delta}\right)^{\alpha}\left(\frac{L}{S_{new}}\right)^{\beta} HFA\right] \tag{13b}$$

$$Y_{new} = a + bX_{new} \tag{13c}$$

The geometry scale, H, is now split into H_1 and H_2 (shown in Figure 8) which are defined as the heights of each adjustable block with respect to the upstream plate - postive values being above the flat plate level. ΔH is the height of the rear face of the cavity, $H_2 - H_1$. In the above formulation, the absolute, scalar height is used.

The term $|\Delta H|/\delta$ appears in both X_{new} and Y_{new}. The height of the fence block H_1 is contained within the S_{new} term. This term was adapted from that used by Lamb in the development of previous cavity heating correlations [28] and is defined, approximately, as the ratio between the cross-sectional area of the separation vortex in a cavity and the perimeter of that vortex. While this ratio is simply defined for regular cavities, for geometries with differing front and rear heights, the non-rectangular cavity cross-section must be factored into the ratio. Equation 14 shows the formulation which accounts for non-zero values of H_2.

Copyright © 2024 by the author(s)

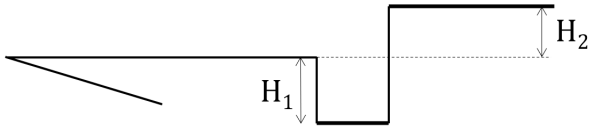

Fig 8. Schematic showing H_1 and H_2 for a stepped-cavity geometry.

$$S_{new} = \frac{L(|H_1| + |\Delta H|)}{L + |H_1| + |\Delta H| + \sqrt{L^2 + (|H_1| - |\Delta H|)^2}} \tag{14}$$

To apply the modified correlation to experimental data, Equation 13 is rearranged for HFA, this is shown in Equation 15:

$$HFA = e^a \left[M_e^\sigma Re_\theta^\tau \left(\frac{|\Delta H|}{\delta} \right) \right]^b \left(\frac{|\Delta H|}{\delta} \right)^{-\alpha} \left(\frac{L}{S_{new}} \right)^{-\beta} \tag{15}$$

Constants are fitted to this equation using the Levenberg-Marquardt least-squares fitting method. Constants α, β, τ, a, and b were calculated while σ was set to 0 due to M_e being constant throughout the current dataset. When applied to the data presented in Figure 7a, the modified correlation produces a much better fit, seen in Figure 7b. Constants for this fit are shown in Table 4 along with the R^2 value for the straight line fit (Equation 13c).

Table 4. Constants for average cavity floor HFA using the modified correlation in Equation 13.

α	β	τ	a	b	R^2
2.5341	-1.0941	0.12235	-4.7466	3.7220	0.98495

3.4.1. Other Geometries

Following the success in fitting data for average cavity floor HFA, other flow quantities can be correlated using the same methodology. Figure 9 shows the quantities plotted according to Equation 13. Table 5 shows the fitted constants and R^2 in each case.

Minimum cavity heating

Minimum cavity floor heating for geometries in which the fence is the lowest point (types DU_F, DU_+, and DU_-) is shown in Figure 9a. Points are coloured according to the height of the rear step, H_2. The minimum heat flux occurs at the most upstream internal corner of a cavity, for example at $x = 150$ mm in Figures 5d, 6e, and 6f.

Peak cavity heating

Peak end wall cavity heating for the same geometry types (DU_F, DU_+, and DU_-) is presented in Figure 9b. This peak in heat flux happens on the upstream external corner of the rear step of the cavity geometry: $x = 155$ mm in Figures 5d, 6e, and 6f.

Minimum separation heating

The minimum heat flux caused by the separation downstream of a step is correlated in Figure 9c. Points are coloured according to fence height, H_1. Geometries included contain a single backward facing element, with either no upstream or positive upstream steps ($H < 0$ and $H_1 \geq 0$). This corresponds to geometry types of FD, UD_F, UD_+, and UD_-. This minimum heating occurs at $x = 155$ mm in Figures 5b, and 6d.

Peak reattachment heating

The correlation for peak heating at the reattachment location following a separation is shown in Figure 9d. As with minimum separation heating, geometries included are ones which experience a separation

Copyright © 2024 by the author(s)

with no intermediate steps or cavities: FD, UD_F, UD_+, and UD_-. However, only cases which produce an overshoot in heat flux at the separation location are included. Figure 6d provides an example of geometries either side of this criterion and the difference in peak reattachment heating between different geometry scales.

Reattachment length

The reattachment distance, or separation length, following a backward facing geometry can also be correlated. The same geometries are used as for peak reattachment heating, with the same restrictions regarding an overshoot at reattachment. Figure 9e shows the correlated data. Unlike each other correlation presented, this time the HFA term in Equation 13b is replaced with a non-dimensional distance term and the Y axis, shown in Equation 16, is defined slightly differently.

$$Y_{new,\,reattach} = \ln\left[\left(\frac{|\Delta H|}{\delta}\right)^{\alpha}\left(\frac{L}{S_{new}}\right)^{\beta}\left(\frac{x_{reattach}-x_{step}}{|\Delta H|}\right)\right] \tag{16}$$

Where $x_{reattach} - x_{step}$ is the distance between the backward facing step and the reattachment location and ΔH is the height of the backward facing step (referring to Figure 8). For the purpose of simplicity, $x_{reattach}$ is defined as the location of the peak in heat flux following a separation: for example, $x_{reattach} \approx 162$ mm in Figure 5c. Figure 6c illustrates different peak heating locations, and therefore different reattachment lengths, for different rear step heights.

Peak step heating

The peak heating on prominent forward facing steps (steps with no upstream intermediate steps or larger downstream steps) is independent on any downstream geometry changes. As such, the only geometry dependent quantity is the initial step height, H_1. Both the X and Y correlation parameters have been redefined to account for this, shown in Equation 17.

$$X_{new,\,step} = \ln\left[M_e^{\sigma} Re_{\theta}^{\tau}\left(\frac{H_1}{\delta}\right)\right] \tag{17a}$$

$$Y_{new,\,step} = \ln\left[\left(\frac{H_1}{\delta}\right)^{\alpha}\left(\frac{L}{S_{new}}\right)^{\beta} HFA\right] \tag{17b}$$

For this formulation, the height terms use H_1 rather than $|\Delta H|$, and the exponent for the second term in the Y axis, β, is set to 0. This correlation is plotted in Figure 9f. Geometries included are types UF, UD_+, UD_F, and UD_- where peak heat flux occurs, for example, at $x = 150$ mm in Figures 5c and 6c.

Table 5. Constants for Equation 13

	Equation	Figure	α	β	τ	a	b	R^2
Minimum cavity	13	9a	2.395	-1.249	0.09848	-4.640	3.826	0.9830
Peak cavity	13	9b	2.561	-1.192	0.07351	-2.882	3.722	0.9907
Minimum separation	13	9c	3.644	0.9613	0.01916	-0.07186	2.649	0.9972
Peak reattachment	13	9d	3.232	0.4312	-0.01397	1.217	3.078	0.9997
Reattachment length	16	9e	3.189	-0.8516	-0.06407	1.910	3.102	0.9996
Peak step	17	9f	3.030	0	-0.06719	3.186	3.257	0.9980

Copyright © 2024 by the author(s)

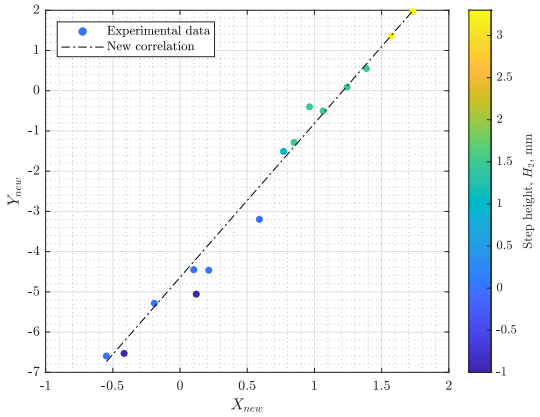

(a) Minimum cavity HFA.

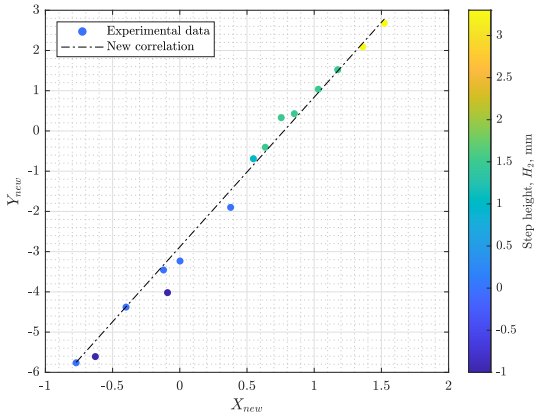

(b) Peak cavity HFA.

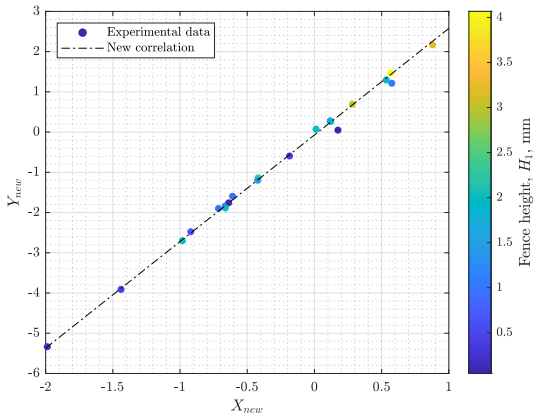

(c) Minimum separation HFA.

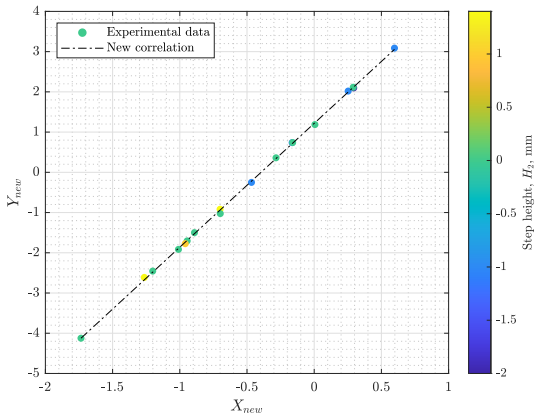

(d) Peak reattachment HFA.

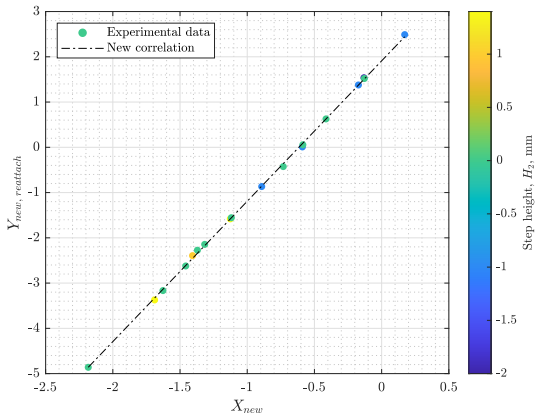

(e) Reattachment location.

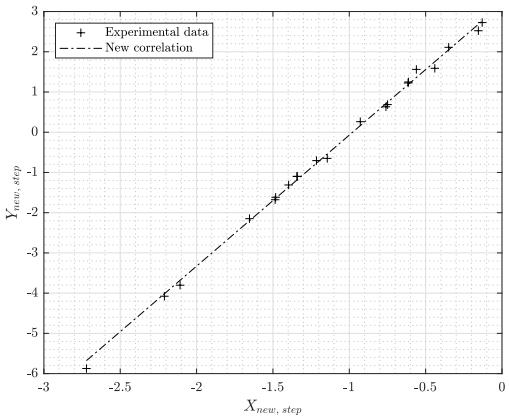

(f) Peak step HFA.

Fig 9. Correlations following Equations 13, 16, and 17.

Copyright © 2024 by the author(s)

4. Conclusions

A wide-ranging heat flux augmentation dataset has been collected for surface imperfections in turbulent boundary layers. A number of quantities, useful for CFD validation, material selection, and aircraft design processes, have been correlated with geometric and flow properties. These correlations are applicable to both better understood simple geometries and more complex combined geometries. A modified version of Everhart's [9] correlation method was the most readily adaptable and has produced the best fit for a range of different geometry categories.

Acknowledgements

Thanks to the European Space Agency for funding this work through contract 4000129548/19/NL/BJ/ig. The authors would also like to thank the tunnel and technical staff at the Oxford Thermofluids Institute whose help and expertise were invaluable in the completion of this work.

References

[1] Steelant, J., Varvill, R., Walton, C., Defoort, S., Hannemann, K., Marini, M.: Achievements obtained for sustained hypersonic flight within the LAPCAT-II project. 20th AIAA International Space Planes and Hypersonic Systems and Technologies Conference, p. 3677 (2015)

[2] Campbell, C., Anderson, B., Bourland, G., Bouslog, S., Cassady, A., Horvath, T., Berry, S., Gnoffo, P., Wood, W., Reuther, J., et al.: Orbiter Return to Flight Entry Aeroheating. 9th AIAA/ASME Joint Thermophysics and Heat Transfer Conference, p. 2917 (2006)

[3] Sandham, N., Van den Eynde, J.: Outcome of high-speed boundary layer transition workshop at HiSST 2022. CEAS Space Journal, pp. 1–3 (2023)

[4] Steelant, J., Passaro, A., Fernandez Villace, V., Gubanov, A., Ivanyushkin, D., Shvalev, Y., Vo-evodenko, N., Marini, M., Di Benedetto, S.: Boundary layer transition assessment on a slender high-speed vehicle. 21st AIAA International Space Planes and Hypersonics Technologies Conference, p. 2133 (2017)

[5] Jacobs, F., Steelant, J.: Temporal Evolution of Transition Onset along Trajectories of Generic Flight Vehicles (2023)

[6] Hoffmann, J.P., Van den Eynde, J., Steelant, J.: An analysis tool for boundary layer and correlation-based transition onset assessment on generic geometries. CEAS Space Journal, pp. 1–23 (2023)

[7] Karsch, M., Van den Eynde, J., Steelant, J.: Linearly combined transition model based on empirical spot growth correlations. CEAS Space Journal, pp. 1–12 (2023)

[8] Everhart, J.L.: Supersonic/hypersonic laminar heating correlations for rectangular and impact-induced open and closed cavities. Journal of spacecraft and Rockets, 46(3):545–560 (2009)

[9] Everhart, J.L., Greene, F.A.: Turbulent supersonic/hypersonic heating correlations for open and closed cavities. Journal of Spacecraft and Rockets, 47(4):545–553 (2010)

[10] Hollis, B.R.: Compression pad cavity heating augmentation on orion heat shield. Journal of thermophysics and heat transfer, 25(3):329–340 (2011)

[11] Estruch, D., MacManus, D.G., Stollery, J., Lawson, N.J., Garry, K.P.: Hypersonic interference heating in the vicinity of surface protuberances. Experiments in Fluids, 49(3):683–699 (2010)

[12] Ivison, W., Hambidge, C., McGilvray, M., Merrifield, J., Steelant, J.: Experimental Investigation of the Effect of Steps and Gaps on Hypersonic Vehicles. The 2nd International Conference on High-Speed Vehicle Science and Technology (2022)

[13] Flinton, A., Merrifield, J., McGilvray, M., Ivison, W., Jacobs, F., Steelant, J.: Numerical Study of Turbulent Phenomena in Hypersonic Boundary Layers from the Presence of Protuberances and Cavities. The 3rd International Conference on High-Speed Vehicle Science and Technology (2024)

[14] Baehr, H.D., Stephan, K.: Heat and Mass Transfer. Springer, Berlin, Heidelberg (2006)

Copyright © 2024 by the author(s)

[15] Astarita, T., Carlomagno, G.M.: Infrared Thermography for Thermo-Fluid-Dynamics. Springer Science & Business Media (2012)

[16] Zaccara, M., Edelman, J.B., Cardone, G.: A general procedure for infrared thermography heat transfer measurements in hypersonic wind tunnels. International Journal of Heat and Mass Transfer, 163:120419 (2020)

[17] Ochs, M., Horbach, T., Schulz, A., Koch, R., Bauer, H.: A novel calibration method for an infrared thermography system applied to heat transfer experiments. Measurement Science and Technology, 20(7):075103 (2009)

[18] Spectroscopy of Atmospheric Gases (2023). URL `https://spectra.iao.ru/home`

[19] Mikhailenko, S., Babikov, Y.L., Golovko, V.: Information-calculating system Spectroscopy of Atmospheric Gases. The structure and main functions. Atmos. Oceanic Opt., 18:685–695 (2005)

[20] Oldfield, M.: Impulse Response Processing of Transient Heat Transfer Gauge Signals. Journal of Turbomachinery (2008)

[21] Ivison, W., Hambidge, C., Doherty, L., McGilvray, M.: Commissioning Ludwieg Mode with Isentropic Compression Heating for the Oxford High Density Tunnel. AIAA SCITECH 2024 Forum, p. 2755 (2024)

[22] Hillyer, J., Doherty, L., Hambidge, C., McGilvray, M.: Enhancing the Test Time Performance of Ludwieg Tunnels. AIAA SCITECH 2024 Forum, p. 2754 (2024)

[23] McGilvray, M., Doherty, L.J., Neely, A.J., Pearce, R., Ireland, P.: The oxford high density tunnel. 20th AIAA international space planes and hypersonic systems and technologies conference, p. 3548 (2015)

[24] Wylie, S., Doherty, L., McGilvray, M.: Commissioning of the Oxford High Density Tunnel (HDT) for Boundary Layer Stability Measurements at Mach 7. 2018 Fluid Dynamics Conference, p. 3074 (2018)

[25] Eckert, E.R.G.: Survey of Boundary Layer Heat Transfer at High Velocities and High Temperatures, vol. 59. Wright Air Development Center, Air Research and Development Command, United … (1960)

[26] Charwat, A., Roos, J., Dewey Jr, F., Hitz, J.: An Investigation of Separated Flows - Part I: The Pressure Field. Journal of the Aerospace Sciences, 28(6):457–470 (1961)

[27] White, F.M., Majdalani, J.: Viscous Fluid Flow, vol. 3. McGraw-Hill New York (2006)

[28] Lamb, J.: Analysis and Correlation of Convective Heat Transfer Measurements of Open Cavities in Supersonic Flow. 15th Thermophysics Conference, p. 1526 (1980)

Copyright © 2024 by the author(s)